NaSICON-type solid-state Li$^+$ ion conductors with partial polyanionic substitution of phosphate with silicate

Asmaa Loutati [a,b,c,*], Olivier Guillon [a,b,d], Frank Tietz [a,b], Dina Fattakhova-Rohlfing [a,b,c]

[a] Forschungszentrum Jülich GmbH, Institute of Energy and Climate Research, Materials Synthesis and Processing (IEK-1), D-52425, Jülich, Germany
[b] Forschungszentrum Jülich GmbH, Helmholtz-Institute Münster (IEK-12), D-52425, Jülich, Germany
[c] University of Duisburg-Essen, Faculty of Engineering, Lotharstr. 1, 47057, Duisburg, Germany
[d] Jülich Aachen Research Alliance, JARA-ENERGY, Germany

ABSTRACT

The increasing demand for safe energy storage has led to intensive investigations of solid-state Li$^+$-ion conductors in the Li_2O-M_2O_3–ZrO_2–SiO_2–P_2O_5 system. As a continuation of the cation substitution in this system, which we reported on very recently, a study of the impact of polyanionic substitutions on ionic conductivity was carried out here in two series, $Li_{3+x}Sc_2Si_xP_{3-x}O_{12}$ ($0 \leq x \leq 0.6$) and $Li_{1.2+x}Sc_{0.2}Zr_{1.8}Si_xP_{3-x}O_{12}$ ($0.3 \leq x \leq 2.8$), with the aim of increasing ionic conductivity, determing the phase stability, and optimizing the processing conditions – especially decreasing the sintering temperatures – depending on the level of substitution.

The polyanionic substitution, i.e. the substitution of $(PO_4)^{3-}$ with $(SiO_4)^{4-}$, in the Li_2O–Sc_2O_3–ZrO_2–SiO_2–P_2O_5 system revealed that a) the sintering temperature can effectively be reduced, b) the presence of zirconium can limit the evaporation of lithium species even at high sintering temperatures, c) the purity of the NaSICON materials has a strong influence on the grain boundary resistance, and therefore on the ionic conductivity, and d) the silicate substitution in $Li_{3+x}Sc_2Si_xP_{3-x}O_{12}$ ($0 \leq x \leq 0.6$) stabilized the monoclinic polymorph (space group $P2_1/n$) with an enhanced total ionic conductivity at 25 °C from 6.5×10^{-7} S cm^{-1} to 1.2×10^{-5} S cm^{-1} for x = 0 to x = 0.15, respectively, exhibiting the highest ionic conductivity at 25 °C among the compositions investigated.

1. Introduction

Solid-state lithium ion conductors are attracting considerable attention from academia and industry as solid electrolytes (SEs) for future all-solid-state Li batteries (ASLBs) [1–4]. The main classes of SEs studied so far include polymers [5,6], sulfides [7,8], and oxide ceramics [7,9,10], which each have individual advantages and disadvantages. Oxide ceramic SEs are characterized by having the widest electrochemical stability window, excellent thermal stability and a wide temperature operation regime, high mechanical strength, and a high level of safety [11–13]. However, their major drawback is that they need to be processed at high temperatures, resulting in high production costs and undesirable reactions with other cell components.

Solid ion conductors with a NaSICON structure (abbreviation for Na$^+$ super ionic conductor) and especially compounds with the general formula $Li_{1+x}Al_xM_{2-x}(PO_4)_3$ (M = Ti, Ge) are promising SEs due to their favorable ionic conductivity at room temperature (RT) [14–17], their relatively low density, and their relatively inexpensive precursor materials, apart of Ge compounds. $Li_{1+x}Al_xTi_{2-x}(PO_4)_3$ (LATP) and $Li_{1+x}Al_xGe_{2-x}(PO_4)_3$ (LAGP) have the highest Li$^+$ ionic conductivities at room temperature in this NaSICON family. A wide range of ionic conductivity from 10^{-5} to 10^{-3} S cm^{-1} has been demonstrated for LATP materials, depending on the stoichiometry, preparation methods, densities, and microstructures of the sintered pellets [13,18–23]. Similarly, LAGP materials exhibit very high ionic conductivity from 10^{-4} to 10^{-3} S cm^{-1} in a wide composition range [19,24–27]. However, the instability of titanium- and germanium-containing compounds against reduction to Ti^{3+} or Ge^{2+} in direct contact with lithium anodes leads to severe performance degradation [20,21]. Therefore, the application of NaSICON-type SEs in ASLBs with a lithium metal anode poses many challenges in terms of interfacial protection [28,29].

Increasing the electrochemical stability of NaSICON-type SEs while

maintaining high ionic conductivity and at the same time significantly lowering the processing temperature and shortening the processing time is not a trivial task. A general strategy for increasing the electrochemical stability is to replace "critical" redox-active ions such as Ti or Ge in the NaSICON structure with redox-inactive ions. Zirconium is the most popular element for this purpose, but the ionic conductivity of Zr-based NaSICONs is far inferior to that of Ti- and Ge-based compounds, and their sintering temperature is usually even higher than that of LATP and LAGP. Therefore, many studies have been carried out to improve the properties of Zr-based NaSICON SEs by partially replacing Zr^{4+} ions with di- or trivalent cations in the general formula $Li_{1+(4-n)x}M^{n+}_xZr^{4+}_{2-x}$ $(PO_4)_3$ when M was Sc [30,31], Y [32,33], Al [34,35], Ca [36,37], Sr [38,39] and Fe, Cr, and In Ref. [40]. In most cases, the crystal symmetries for NaSICON materials with the above cation substitutions are the rhombohedral modification (space group $R\bar{3}c$), which has the highest ion conductivity [31]; orthorhombic (space group *Pbcn*) [29]; monoclinic (space group $P2_1/n$) [41]; and occasionally triclinic (space group $P\bar{1}$) [42], depending on composition, synthesis conditions, and temperature. However, a long sintering time (up to 10 h) at high temperatures (above 1200 °C) [43] is required to stabilize the rhombohedral phase, which results in high total ionic conductivity, but easily leads to undesired micro-crack formation when cooling from the high temperature [44,45]. In addition, the loss of volatile lithium species at high sintering temperatures [46] is the reason for the increased pore formation [22]. All these aspects eventually lead to the deterioration of ionic conductivity. Moreover, prolonged sintering at high temperatures inevitably increases production costs. Therefore, there is an urgent need to lower the sintering temperatures of Zr-containing NaSICON materials, either through the addition of sintering aids [46,47] or by changing the composition. The second approach is particularly appealing, as it would avoid the addition of the second phase, which may eventually lead to inhomogeneities in the composition, microstructure, and deteriorating electrochemical and mechanical properties. The main strategy in this investigation is polyanionic substitution. Existing examples of this approach include NaSICON materials with the partial substitution of phosphorous with silicon ($Li_{3+x}Sc_2Si_xP_{3-x}O_{12}$ with $0 \leq x \leq 0.6$) [48] and with additional Zr deficiency ($Li_{2.8}Zr_{2-x}Si_{1.8-4x}P_{1.2+4x}O_{12}$ with $0 \leq x \leq 0.45$) [49].

In this work, two series of compounds belonging to the $Li_{1+x+y}Sc_xZr_{2-x}(SiO_4)_y(PO_4)_{3-y}$ system with $x + y \leq 3$ [51] were investigated with the aim of reducing the sintering temperature and increasing the ionic conductivity (see Fig. 1):

a) The $Li_{3+x}Sc_2Si_xP_{3-x}O_{12}$ series with $0 \leq x \leq 0.6$ derived from the parent compound $Li_3Sc_2(PO_4)_3$ (LSP; x = 0). Beyond x = 0.6, the conductivity is expected to decrease due to the declining number of vacancies [52].

b) Partial substitution of P^{5+} with Si^{4+} in the $Li_{1.2+x}Sc_{0.2}Zr_{1.8}Si_xP_{3-x}O_{12}$ system with $0 \leq x \leq 2.8$. The series is an extension of the investigation in the same system with the cation substitution in the solid solution $Li_{1+x}Sc_xZr_{2-x}P_3O_{12}$. The $Li_{1.2}Sc_{0.2}Zr_{1.8}P_3O_{12}$ composition showed the highest conductivity (2.7×10^{-5} S cm^{-1}) within this series (see Ref. [50]).

2. Experimental procedure

2.1. Powder preparation

Stoichiometric amounts of Li_2CO_3 (Alfa Aesar, 99%), ZrO_2 (Saint-Gobain, 99.8%), Sc_2O_3 (Projector, 99.5%), and SiO_2 (Alfa Aesar, 99.8%) were mixed in a quartz glass container and water was used as solvent. After the carbonates were dissolved, a small amount of nitric acid was added to obtain a homogeneous aqueous suspension followed by a stoichiometric amount of $NH_4H_2PO_4$ (Merck, 99%) and stirred overnight at 250 rpm and a temperature of 70 °C for the slow evaporation of
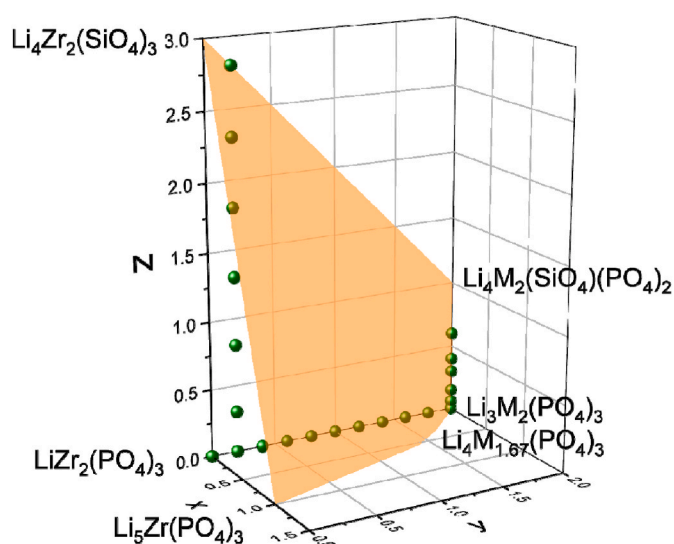

Fig. 1. Exploratory research of NaSICON materials in the Li_2O–M_2O_3–ZrO_2–SiO_2–P_2O_5 system. The orange surface corresponds to the theoretical compositional limits of the NaSICON materials according to the formula $Li_{1+4x+y+z}Zr_{2-x-y}M^{3+}_y(SiO_4)_z(PO_4)_{3-z}$. The end members at the corners of the orange surface are given as chemical formulas. The green dots indicate the investigated samples. In Ref. [50] the horizontal dots from $LiZr_2(PO_4)_3$ to $Li_3M_2(PO_4)_3$, (M = Al, Y, Sc) are reported. In this work, only the compositions of the vertical dots are investigated and discussed. (For interpretation of the references to colour in this figure legend, the reader is referred to the Web version of this article.)

water to form a homogeneous precipitate. Subsequently, the entire homogenized mixture was first heated up to 100 °C and then the dried solid mixture was fired in an oven at 300 °C for 5 h to form an amorphous raw powder. The desired materials were obtained after subsequent calcination at 600 °C for 5 h and final sintering in Pt crucibles.

2.2. Milling

The calcined powders were manually ground in an agate mortar and the powders were then milled in a grinding bowl using ethanol and 5 mm zirconia balls in a planetary ball mill (Fritsch Pulverisette 7 premium line) at 350 rpm for 5 h, before being subsequently dried at 70 °C for 6 h. The particle size distribution was measured using a Horiba LA-950V2 laser diffraction particle size analyzer with ethanol as the dispersing medium.

2.3. Chemical analysis

The stoichiometry of the powders was controlled before and after sintering by inductively coupled plasma optical emission spectroscopy (ICP-OES) using a Thermo Scientific iCAP7600 spectrometer with optical scale and CID semi-conductor detector, axial und radial reflection, and wavelengths between 166 nm and 847 nm. 50 mg of calcined powder was mixed with 0.5 g lithium borate in a platinum crucible and fired for 1 h at 1000 °C in a muffle furnace. The liquefied material was dissolved in 30 mL HCl (5%). After dissolution, the sample solutions were transferred to sample vials containing 0.5 mL HF and filled to a volume of 50 mL. This measurement was performed twice for each composition.

2.4. Thermal analysis

Differential thermal analysis and thermogravimetry (DTA/TG) measurements were carried out on the calcined powders using the STA449F1 Jupiter calorimeter coupled to the QMS 403C Aëolos mass

spectrometer from NETZSCH-Gerätebau GmbH. The measurements were recorded in the temperature range of 25 °C–1600 °C in air with heating and cooling rates of 300 K/h. The dilatometry experiments were performed with a 402C dilatometer also from NETZSCH-Gerätebau GmbH. During the measurements, the shrinkage was recorded until a shrinkage of ~25% was reached.

2.5. Pellet sintering

The calcined and freshly milled powders were pressed into pellets with a pressure of about 150 MPa and sintered in Pt crucibles. The sintering temperatures were obtained from the shrinkage curves of the dilatometer measurements. The experimental density was determined geometrically after sintering and the theoretical density was obtained from the X-ray diffraction (XRD) refinement results.

2.6. Crystallography

The phase purity of the sintered specimens was measured by XRD from $2\theta = 10°$–60° with a step size of 0.02° and a dwell time of 0.75 s. The measurements were recorded with a Bruker D4 Endeavor diffractometer using Cu K$_\alpha$ radiation. The Rietveld refinements for the determination of the lattice parameters of the resulting compounds were performed using the TOPAS V.4.2 (Bruker AXS 2008, Germany) computer software.

Depending on the composition, synthesis conditions, and temperature, the prevalent crystal structure for lithium-based NaSICON materials is most commonly reported as either rhombohedral, monoclinic, orthorhombic, or triclinic. In this work, the powder XRD patterns of materials in both the $Li_{3+x}Sc_2Si_xP_{3-x}O_{12}$ and $Li_{1.2+x}Sc_{0.2}Zr_{1.8}Si_xP_{3-x}O_{12}$ series were indexed with a monoclinic or an orthorhombic structure. In order to determine the exact structure of the materials, a comparison of the XRD patterns of different relevant NaSICON materials reported in the literature with monoclinic structure (space group $P2_1/n$) or orthorhombic structure (space groups $Pbcn$, $Pbna$, $Pcan$) are compiled and presented in Fig. 2. The figure clearly shows that the XRD patterns of monoclinic and orthorhombic structures are nearly identical. The

authors in Ref. [29] explain that the two polymorphs can be distinguished by two small reflections (see black arrows), but other compositions they refined with both structures resulting in same quality of the fitted patterns, whereas in other references this difference in the patterns is not observed. Therefore, it is nearly impossible to distinguish between the two symmetries, which was also observed and confirmed by others [56].

2.7. Electrical characterization

For conductivity measurements, a VMP-300 multi-potentiostat (BioLogic) combined with a climate chamber (Vötsch VT4002EMC) was used. Impedance spectra were measured in the frequency range from 7 MHz to 1 Hz. Prior to the measurements, both sides of the prepared dense pellets were dry-polished using SiC sandpapers up to 4000 grit and then sputter-coated with gold as blocking electrodes using a Cressington 108 coater. ZView software (Scribner Associates Inc) was used to analyze the impedance spectra.

3. Results and discussion

3.1. $Li_{3+x}Sc_2Si_xP_{3-x}O_{12}$ $(0 \leq x \leq 0.6)$

Powders belonging to the $Li_{3+x}Sc_2Si_xP_{3-x}O_{12}$ system with $0 \leq x \leq 0.6$ were synthesized via solution-assisted solid-state reaction (SA-SSR), as previously reported [51]. The ICP-OES results confirmed the nominal stoichiometry of the six calcined NaSICON $Li_{3+x}Sc_2Si_xP_{3-x}O_{12}$ powders with x = 0, 0.06, 0.15, 0.3, 0.4, and 0.6. The analytical values are very close to the targeted compositions after powder preparation, i.e. the substitution of P^{5+} with Si^{4+} was successful with a high level of precision (Table 1). The obtained atomic ratios were normalized to two moles scandium per formula unit. With the exception of $Li_3Sc_2P_3O_{12}$, the silicone and phosphorous contents deviate less than the experimental error (3%). The lithium content was slightly lower than anticipated, which might be due to the uptake of small amounts of water in the Li_2CO_3 during storage.

DTA/TG measurements were carried out up to 1600 °C to analyze the formation and stability of the crystalline phase, to quantify mass losses, and to identify the melting points. Materials of the studied series $Li_{3+x}Sc_2Si_xP_{3-x}O_{12}$ $(0 \leq x \leq 0.6)$ have almost the same thermal behavior except for the material with x = 0.6. The TG curves show three successive mass losses accompanied by endothermic signals. As shown in Fig. 3a and b, the first mass loss $\Delta m_1 \approx 0.9\%$ was observed in the temperature range from 25 °C to 250 °C and is mainly associated with physisorbed water, whereas the second mass loss $\Delta m_2 \approx 2\%$ occurred up to 560 °C in two steps accompanied by an endothermic signal peaking around 330 °C, which has been attributed to the release of crystal water from the materials. Furthermore, the third loss $\Delta m_3 \approx 2.6\%$ appeared in the temperature range from 1300 °C to 1600 °C and is ascribed to the evaporation of lithium oxide from the material [57]. The evaporation of lithium oxide is pronounced when the materials are fully molten. The broad exothermic signal between 400 °C and 600 °C, which is not accompanied by mass loss, is interpreted as the phase formation and
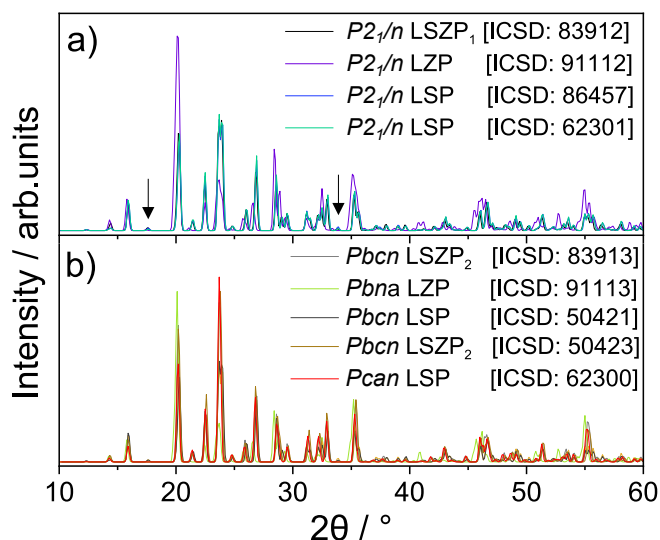

Fig. 2. XRD patterns for reported NaSICON materials with a) monoclinic symmetry (space group $P2_1/n$): $Li_{2.96}(Sc_{1.96}Zr_{0.04})(PO_4)_3$ (LSZP1) [ICSD N°: 83912] [29], $LiZr_2(PO_4)_3$ (LZP) [ICSD N°: 91112] [53], $Li_3Sc_2(PO_4)_3$ (LSP) [ICSD N°: 86457] [54], and LSP [ICSD N°: 62301] [40], and b) orthorhombic symmetry (space groups $Pbcn$, $Pbna$, or $Pcan$): $Li_{2.8}(Sc_{1.8}Zr_{0.2})(PO_4)_3$ (LSZP2) [ICSD N°: 83913] [29], LSP [ICSD N°: 50421] [30], LSZP2 [ICSD N°: 50423] [30], LZP [ICSD N°: 91113] [53], and LSP [ICSD N°: 62300] [55].

Table 1
Composition of the $Li_{3+x}Sc_2Si_xP_{3-x}O_{12}$ $(0 \leq x \leq 0.6)$ NaSICON powders calcined at 600 °C for 5 h determined by ICP-OES and normalized to 2 mol scandium per formula unit. The oxygen content was calculated on the basis of the cation contents.

X	Analytical stoichiometry before sintering
0	$Li_{2.98}Sc_2P_{2.9}O_{11.74}$
0.06	$Li_{3.04}Sc_2Si_{0.08}P_{2.96}O_{12.08}$
0.15	$Li_{3.14}Sc_2Si_{0.18}P_{2.83}O_{12.01}$
0.3	$Li_{3.26}Sc_2Si_{0.33}P_{2.72}O_{12.09}$
0.4	$Li_{3.37}Sc_2Si_{0.38}P_{2.62}O_{12}$
0.6	$Li_{3.57}Sc_2Si_{0.59}P_{2.41}O_{11.99}$

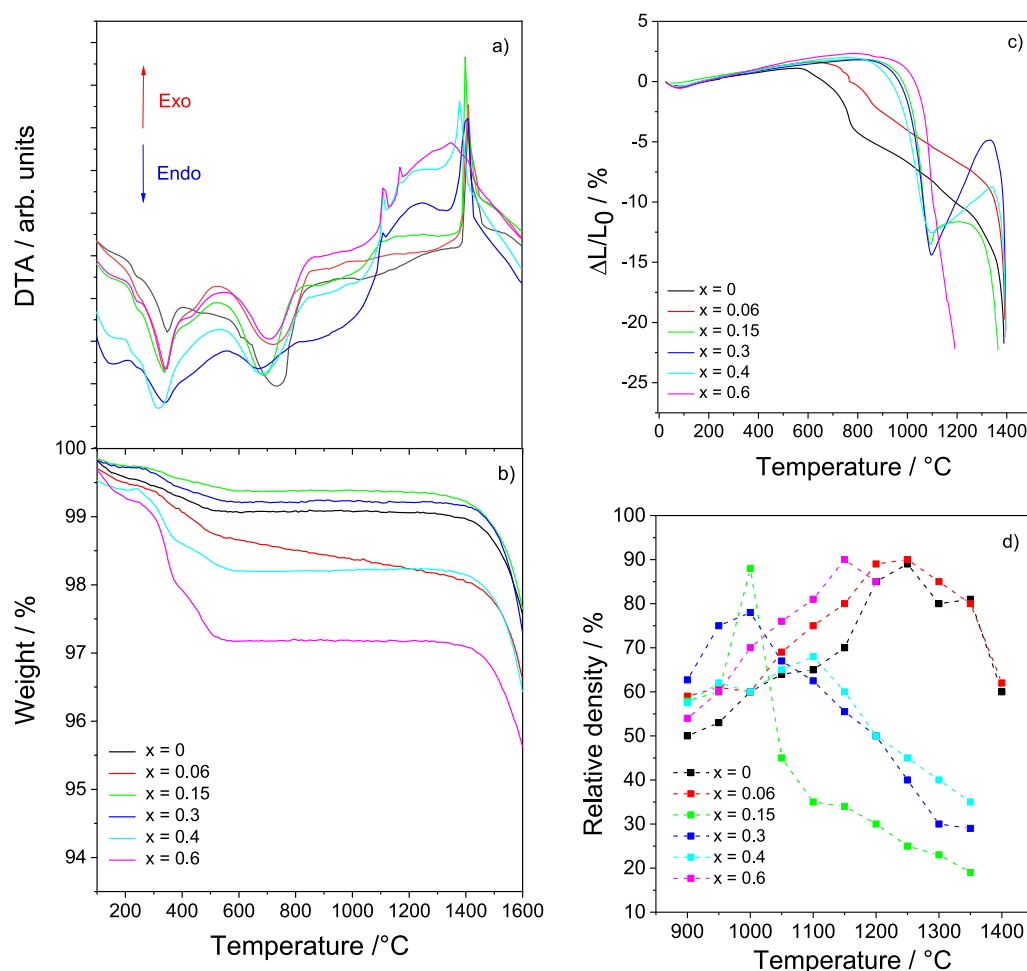**Fig. 3.** Thermal and dilatometry investigations of the $Li_{3+x}Sc_2Si_xP_{3-x}O_{12}$ series ($0 \leq x \leq 0.6$): **a)** DTA results, **b)** TG results, **c)** sintering curves of samples with a constant heating rate up to 1600 °C, **d)** relative densities obtained after sintering (3 h) at different sintering temperatures.

crystallization region of the materials. Very sharp exothermic signals were detected at around 1400 °C, which are ascribed to the melting point of the materials with $0 \leq x \leq 0.4$, whereas the sample with x = 0.6 showed a partial melting point at 1100 °C followed by complete melting at 1170 °C. Weak signals at these two temperatures were also observed for x = 0.3 and x = 0.4. In fact, the increased silicate substitution in the $Li_{3+x}Sc_2Si_xP_{3-x}O_{12}$ series leads to a decrease of the melting temperature. This result is in agreement with previous observations [48].

Dilatometry was used to determine the optimal sintering temperature of the materials. In order to obtain full density for a typical pellet with a green density of 50%, a theoretical final value of 20.6% shrinkage is necessary. Larger shrinkage values obtained in dilatometer measurements indicate a (partial) melting of the material or a continuous plastic deformation of the sample induced by the low pressure of the push-rod [58]. The shrinkage behavior of the pellets of the $Li_{3+x}Sc_2Si_xP_{3-x}O_{12}$ series with x = 0, 0.06, 0.15, 0.3, 0.4, and 0.6 was recorded during constant heating (300 K/h) until a shrinkage of around 23% was reached (Fig. 3c). The shrinkage behavior of the samples strongly varies with increasing silicate content (Fig. 3c). The samples with x = 0 and x = 0.06 show rather sluggish shrinkage at temperatures up to 1300 °C and a steep slope at about 1370 °C indicating their melting. Materials with $0.15 \leq x \leq 0.4$ exhibit shrinkage up to ~15% at 1050 °C followed by expansion until 1250 °C, 1320 °C, and 1340 °C for compositions with x = 0.15, 0.3, and 0.4, respectively.

To achieve the optimum sintering conditions for each composition, the pressed pellets were sintered in air at different temperatures. The

highest temperature was initially determined from the dilatometry measurements and optimized by lowering it by 50 °C in the subsequent tests. The sintering experiments in the furnace were carried out between 900 °C and 1400 °C for materials with x = 0 and x = 0.06, between 900 °C and 1350 °C for materials with x = 0.15, 0.3, and 0.4, and only from 900 °C to 1200 °C for the material with x = 0.6, since the pellets already melted at about 1220 °C. After several sintering tests in the same oven and under the same conditions (3 h, 300 K/h cooling and heating), the optimal sintering temperatures that yielded the highest relative densities were determined and are listed in Table 2. No significant shrinkage was observed below the given temperatures, while some micro-cracks were observed above them for compositions with x = 0, 0.06, and 0.6. The sintering experiments in the furnace revealed a systematic decrease in density with increasing sintering temperature for compositions with x = 0.15, 0.3, and 0.4. The reason for this trend is the volume expansion, which was already recorded by dilatometry in connection with deformations and the partial melting of the pellets. The relative densities obtained at different sintering temperatures from 900 °C to 1400 °C are shown in Fig. 3d.

In an attempt to further increase the relative density of the sintered pellets, an optimized two-step sintering procedure was applied [59]. The pellets were first subjected to the optimum sintering temperatures determined above (Table 2) for a short period of time (0.25 h) and then annealed at a reduced temperature for a longer period of time (4 h). The sintering conditions were systematically optimized by varying the second temperature in the range of 700 °C–1000 °C for materials with x =

Table 2

Melting points determined by DTA measurements, sintering parameters for the one-step sintering and two-step sintering (T_s = sintering temperature, t_s = dwell time), and the resulting densities of $Li_{3+x}Sc_2Si_xP_{3-x}O_{12}$ ($0 \leq x \leq 0.6$) compounds.

Composition	Melting temperature/°C	One-step sintering			Two-step sintering		
		T_s/°C, t_s/h		Relative density/%	T_{s1}/°C, t_{s1}/h	T_{s2}/°C, t_{s2}/h)	Relative density/%
$Li_3Sc_2P_3O_{12}$	1410	1250, 3		89	1250, 0.25	800, 4	96
$Li_{3.06}Sc_2Si_{0.06}P_{2.94}O_{12}$	1410	1250, 3		90	1250, 0.25	800, 4	94
$Li_{3.15}Sc_2Si_{0.15}P_{2.85}O_{12}$	1390	1000, 3		88	1000, 0.25	800, 4	93
$Li_{3.3}Sc_2Si_{0.3}P_{2.7}O_{12}$	1100, 1390	1000, 3		78	1000, 0.25	800, 4	85
$Li_{3.4}Sc_2Si_{0.4}P_{2.6}O_{12}$	1100, 1380	1100, 3		68	1100, 0.25	800, 4	82
$Li_{3.6}Sc_2Si_{0.6}P_{2.4}O_{12}$	1100, 1170	1150, 3		90	1150, 0.25	800, 4	96

0 and x = 0.06 with 50 °C steps and in the range of 700 °C–900 °C with 50 °C steps for materials with x = 0.15, 0.3, 0.4, and 0.6. The relative density of the pellets was thus increased for all compositions (Table 2).

It should be noted that the NaSICON solid electrolyte is highly susceptible to Li_2O loss during conventional sintering, which typically requires higher temperatures of about 1200 °C and a longer dwell time of several hours [34]. The lower sintering temperature and shorter dwell time are expected to minimize the Li_2O evaporation, resulting in higher conductivity [60]. In contrast, higher sintering temperatures typically lead to a higher relative density, which also has a positive effect on ionic conductivity. The combination of these two approaches is the key to manufacturing solid electrolytes with high ionic conductivity [61].

In order to evaluate the possible Li_2O loss after one-step and two-step sintering, the pellets were analyzed by ICP-OES. As can be seen in Fig. 4, the lithium content is lower than anticipated in all cases. However, Li_2O loss can be limited by performing a two-step sintering procedure and the reduction of Li_2O loss is clearly seen in Fig. 4.

During the two-step sintering procedure, the materials were annealed with shorter times compared to the conventional sintering process used by Peng et al. [48], in which the pressed pellets of the materials were sintered for 6 h. The lower temperature and shorter times likely result in less Li_2O loss, which, in turn, should result in higher grain

boundary conductivity, as suggested by Ban et al. [62]. Therefore, the use of a two-step sintering procedure not only reduces the energy input and increases the relative density of the pellets, but also minimizes the loss of Li_2O due to the short dwell time at a high temperature [58,59]. This heat treatment sequence was thus applied to sinter all samples for further investigations.

XRD patterns (Fig. 5) of the studied materials $Li_{3+x}Sc_2Si_xP_{3-x}O_{12}$ ($0 \leq x \leq 0.6$) recorded after two-step sintering (Table 2) exhibit reflections of the orthorhombic structure (space group *Pbcn*, ICSD No. 83913) [29] and/or reflections of the monoclinic structure (space group *P2₁/n*, ICSD No. 91112) [53], since both phases are almost identical and resemble each other in their reflection patterns, as shown in Fig. 2. However, since the two small reflections at 2θ = 17.7° and 34° could hardly be detected in all XRD patterns, the lattice parameters (see Fig. 6) were determined with the monoclinic.

Moreover, a small amount of secondary phase such as orthorhombic Li_3PO_4 (ICSD No. 50058) (space group *Pmnb*) [63] in the compositions x = 0.4 and x = 0.6 were found as mentioned in Refs. [38,64]. Cubic Sc$(PO_3)_3$ (ICSD No. 1719) (space group $I\bar{4}3d$) was also detected as an impurity in the material with x = 0.6 [65]. For the unsubstituted LSP, a very small amount of rhombohedral P_2O_5 (ICSD No. 16610) [66] remained unreacted during the synthesis, as also reported in previous work [31,55], and unreacted monoclinic Sc_2O_3 (space group *C2/m;* ICSD no. 160218) [67] was also detected. However, for the same
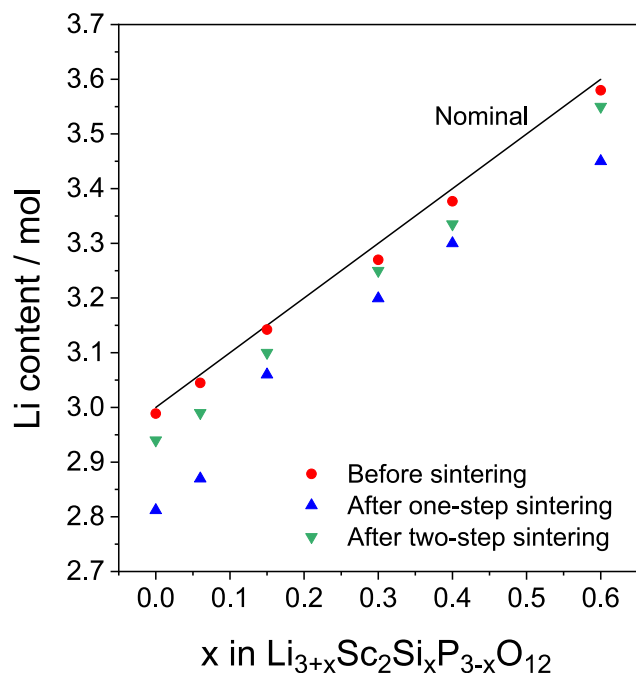

Fig. 4. Variation of lithium content obtained from ICP-OES in the $Li_{3+x}Sc_2Si_xP_{3-x}O_{12}$ series ($0 \leq x \leq 0.6$) before sintering, after one-step sintering, and after two-step sintering. The results were normalized to 2 mol scandium per formula unit. The pellets were sintered at the temperatures listed in Table 2. Symmetry in accordance with [30].
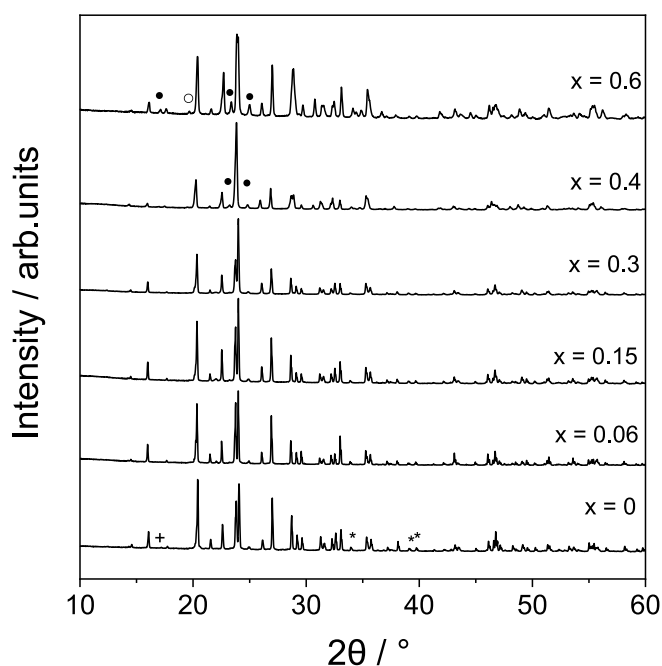

Fig. 5. XRD patterns of $Li_{3+x}Sc_2Si_xP_{3-x}O_{12}$ ($0 \leq x \leq 0.6$) after two-step sintering (see Table 2). ○: Sc$(PO_3)_3$, +: P_2O_5, ●: Li_3PO_4, *: Sc_2O_3. is the main phase for all samples with small amounts of an unidentified impurity phase [48].
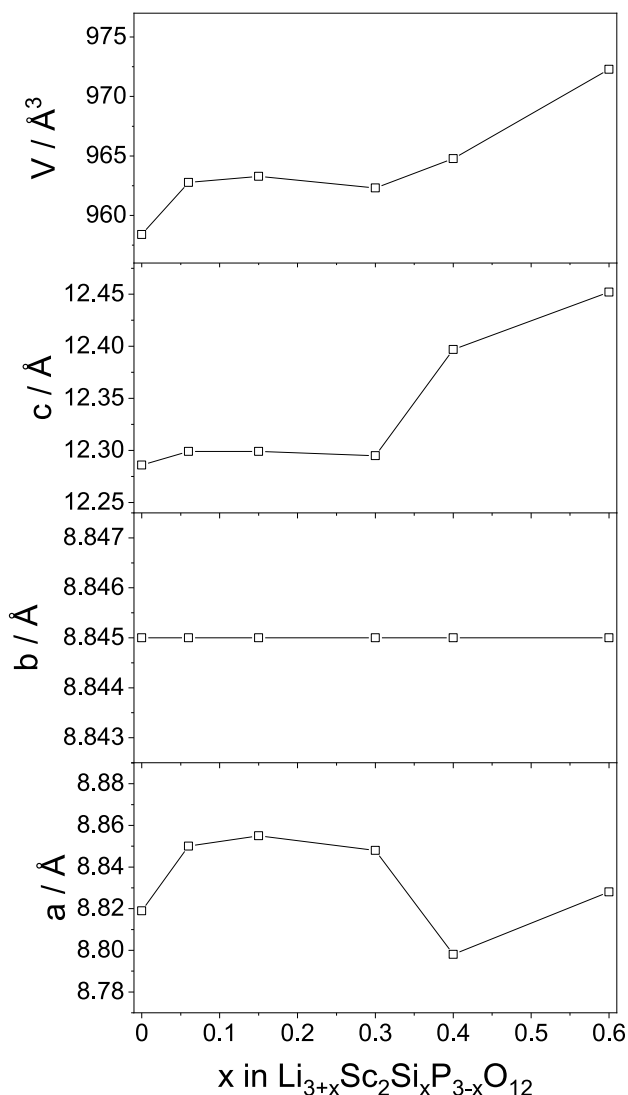
Fig. 6. Variation of monoclinic lattice parameters and unit cell volume of the $Li_{3+x}Sc_2Si_xP_{3-x}O_{12}$ series ($0 \leq x \leq 0.6$).

$Li_{3+x}Sc_2Si_xP_{3-x}O_{12}$ series, it was previously detected that "$Li_{3.2}Sc_2(PO_4)_3$"

The materials in the $Li_{3+x}Sc_2Si_xP_{3-x}O_{12}$ series demonstrate a non-linear dependence of monoclinic lattice parameters and the unit cell volume on the silicate substitution. The unit cell volume increases slightly up to x = 0.06, remains nearly constant up to x = 0.3, and increases for higher x values. The lattice parameter *a* increases slightly up to x = 0.3, decreases at x = 0.4, and increases again at x = 0.6, but *b* remains constant (Fig. 6, the crystallographic data refined with orthorhombic and monoclinic symmetry are listed in Tables S1 and S2 in the supporting information, respectively). The β angle is in the range of $89.8° \leq β \leq 90.2°$, thus indicating the close proximity to the orthorhombic setting.

The variation of the monoclinic lattice parameters during the progressive anionic substitution of $(PO_4)^{3-}$ by $(SiO_4)^{4-}$ is not primarily due to the different ionic radii of Si^{4+} (0.26 Å) and P^{5+} (0.17 Å) in the tetrahedral coordination [68], as this does not necessarily lead to a small volume increase of the tetrahedra. The electrostatic redistribution of charges and the additional uptake of Li^+ ions are more important factors here.

The ionic conductivity of the six compositions studied was

determined from impedance spectra measured at 25 °C. The Nyquist plot of the impedance spectra is shown in Fig. 7a, and the equivalent circuit used is also shown. For all samples, only one semicircle emanating from the origin at high frequencies and a straight line at low frequencies corresponding to the electrode polarization were observed.

The radius of the semicircle decreases with increasing silicate substitution in $Li_{3+x}Sc_2Si_xP_{3-x}O_{12}$ up to x = 0.15 and subsequently increases again. Phenomenologically, the sample with x = 0.15 thus shows the highest ionic conductivity along the series. From the capacities of the semicircles the relative permittivity constants were calculated (see Fig. S1 in the supporting information).

The total conductivity of the samples was calculated with Equation (1):

$$\sigma = \frac{L}{A\,R} \qquad\qquad \text{Equation 1}$$

In which L and A represent the pellet thickness and electrode surface area of the specimen, respectively, and R is the total resistance derived from the fitted impedance spectra. The total ionic conductivity values at 25 °C as a function of composition are listed in Table 3, and the evolution of the total ionic conductivity is shown in Fig. 7b. The total ionic conductivity initially increases with increasing x, and the maximum value of 1.2×10^{-5} S cm^{-1} was obtained with $Li_{3.15}Sc_2Si_{0.15}P_{2.85}O_{12}$. The observed increase in total conductivity can be mainly attributed to the substitution of silicate in $Li_{3+x}Sc_2Si_xP_{3-x}O_{12}$ and the additional Li^+ ions needed for charge balance. Consequently, more lithium ions led to a significant improvement in ionic conductivity.

The subsequent decrease in ionic conductivity can be attributed to two reasons. On the one hand, further increasing the lithium and silicate content seems to destabilize the NaSICON structure and generate an increasing amount of Li_3PO_4, especially for the composition with x = 0.6. On the other hand, the highest ionic conductivity value can also be attributed to the densification process and the quality of the ceramic material. Even when the lithium content is increased, the compositions with x = 0.3 and x = 0.4 exhibit poor ionic conductivity due to their low relative density. It is known that samples with a density below 90% can easily lose up to 90% of their ionic conductivity [46]. Therefore, the potential conductivity of $Li_{3.3}Sc_2Si_{0.3}P_{2.7}O_{12}$ and $Li_{3.4}Sc_2Si_{0.4}P_{2.6}O_{12}$ may be about one order of magnitude higher than was measured. The results are very similar to those of Peng et al. [48]. The ionic conductivity of LSP is lower compared to some of the reported values in the literature [29,30,32,48,56,69–71]. The activation energy E_a of the ionic conductivity of all compounds was obtained from impedance measurements at different temperatures and using the Arrhenius law (Equation (2)), where σ_t is the total conductivity at the absolute temperature T, A is a pre-exponential constant containing the number of charge carriers, jump distance and attempt frequency and k is the Boltzmann constant.

$$\sigma_t T = A e^{-\frac{E_a}{kT}} \qquad\qquad \text{Equation 2}$$

The activation energy values were calculated from the slope of ln σ_tT versus inverse temperature in the temperature range of −40 °C–100 °C as shown in Fig. 7c. The calculated values of E_a after linear fitting are summarized in Table 3. The activation energy of $Li_{3+x}Sc_2Si_xP_{3-x}O_{12}$ specimens varies between 0.19 eV and 0.24 eV without any clear trend. These values are comparable with literature data of other NaSICON-type materials [e.g. 12,18,20,49].

Overall, optimizing the sintering conditions resulted in increased ionic conductivity along the $Li_{3+x}Sc_2Si_xP_{3-x}O_{12}$ series compared to the data reported by Peng et al. [48]. Nevertheless, the obtained ionic conductivities are still too low for battery applications.

3.2. $Li_{1.2+x}Sc_{0.2}Zr_{1.8}Si_xP_{3-x}O_{12}$ ($0 \leq x \leq 2.8$)

The powders belonging to the $Li_{1.2+x}Sc_{0.2}Zr_{1.8}Si_xP_{3-x}O_{12}$ system ($0 \leq x \leq 2.8$) were also synthesized by SA-SSR. The ICP-OES results are summarized in Table 4. The obtained atomic ratios were normalized to
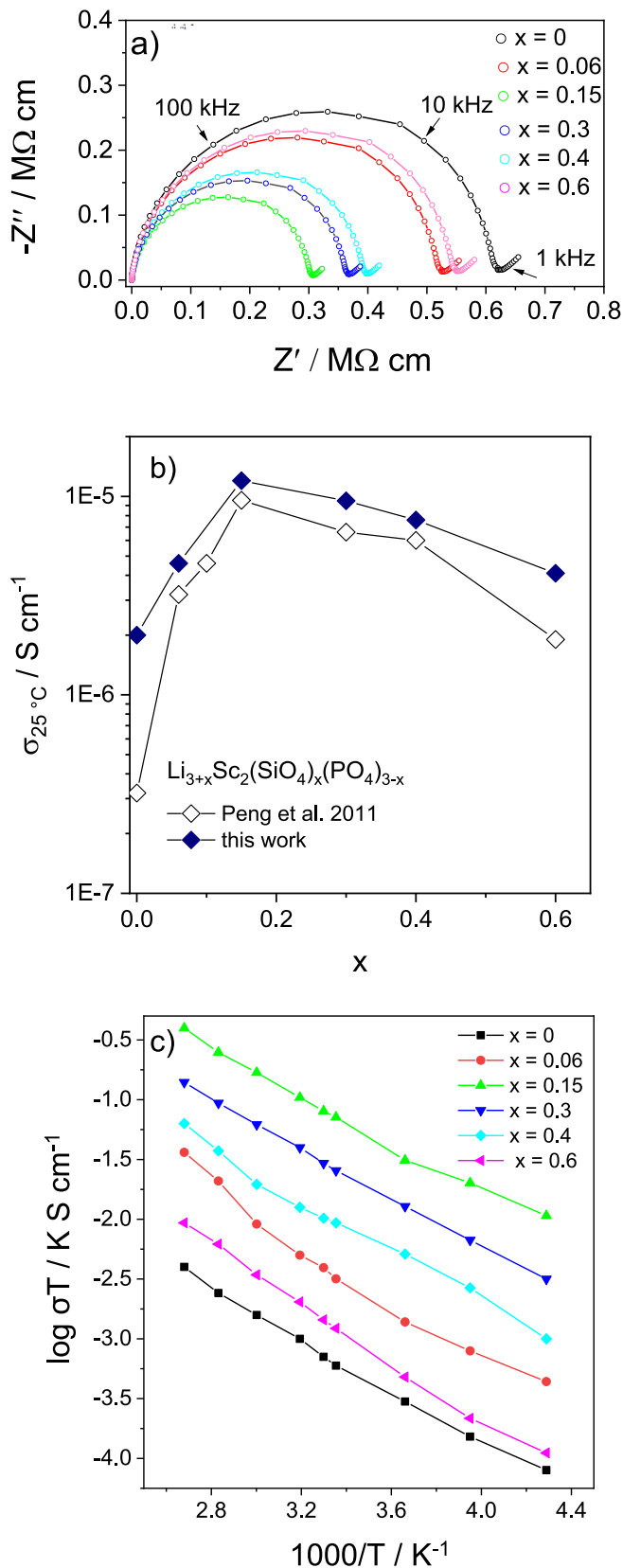
Fig. 7. a) Nyquist plot of impedance spectra at 25 °C after accounting for the sample dimensions. The equivalent circuit for data fitting is also shown. b) Total ionic conductivity at 25 °C depending on the silicate content in $Li_{3+x}Sc_2Si_xP_{3-x}O_{12}$ ($0 \leq x \leq 0.6$). c) Arrhenius plot of σ_t of $Li_{3+x}Sc_2Si_xP_{3-x}O_{12}$ ($0 \leq x \leq 0.6$) measured in the temperature range of −40 °C–100 °C.

Table 3

Resulting densities of ceramics densified in two sintering steps, ionic conductivity at 25 °C and activation energy for $Li_{3+x}Sc_2Si_xP_{3-x}O_{12}$ ($0 \leq x \leq 0.6$).

X	Relative density/%	$\sigma_{25°C}$/S cm^{-1}	Activation energy/eV
0	96	0.2×10^{-5}	0.21
0.06	94	0.46×10^{-5}	0.24
0.15	93	1.20×10^{-5}	0.19
0.3	85	0.95×10^{-5}	0.20
0.4	82 3	0.76×10^{-5}	0.21
0.6	96	0.41×10^{-5}	0.24

Table 4

Composition of $Li_{1.2+x}Sc_{0.2}Zr_{1.8}Si_xP_{3-x}O_{12}$ powders with $0 \leq x \leq 2.8$ calcined at 600 °C determined by ICP-OES and normalized to 1.8 mol zirconium per formula unit. The oxygen content was calculated on the basis of the cation contents.

x	Analytical stoichiometry before sintering
0	$Li_{1.21}Sc_{0.21}Zr_{1.8}P_{3.02}O_{11.99}$
0.3	$Li_{1.53}Sc_{0.21}Zr_{1.8}Si_{0.31}P_{2.70}O_{12.01}$
0.8	$Li_{2.02}Sc_{0.20}Zr_{1.8}Si_{0.75}P_{2.08}O_{12}$
1.3	$Li_{2.60}Sc_{0.19}Zr_{1.8}Si_{1.27}P_{1.71}O_{11.98}$
1.8	$Li_{2.95}Sc_{0.19}Zr_{1.8}Si_{1.78}P_{1.31}O_{12.02}$
2.3	$Li_{3.59}Sc_{0.21}Zr_{1.8}Si_{2.28}P_{0.75}O_{11.99}$
2.8	$Li_{4.11}Sc_{0.21}Zr_{1.8}Si_{2.82}P_{0.22}O_{12.01}$

1.8 mol zirconium per formula unit. The final compositions of the calcined solid electrolyte powders are close to the nominal stoichiometry.

The coupled thermogravimetric DTA/TG study shows that the six Si-containing materials, chosen from the $Li_{1.2+x}Sc_{0.2}Zr_{1.8}Si_xP_{3-x}O_{12}$ ($0.3 \leq x \leq 2.8$) system, clearly have the same thermal behavior except for the material with the lowest silicate content (x = 0.3), as shown in Fig. 8a and b. The TG curves show four temperature regions with mass losses.

The first weight loss occurs below 200 °C and is attributed to the release of moisture. The second weight loss starts at about 300 °C and can be attributed to the evaporation of crystal water and the emission of carbon dioxide. In the DTA curves, this weight loss is accompanied by the presence of an endothermic broad signal centered at 350 °C. This endothermic signal was detected for all compositions except for x = 1.8 and x = 2.3. The third weight loss between 800 °C and 950 °C only affects the powders with x = 2.3 and x = 2.8 and is associated with an endothermic signal at about 950 °C and 980 °C, respectively. This endothermic peak is very likely a partial melting of these two samples and the reason for the first strong shrinkage in the dilatometry curves (Fig. 8c). The fourth weight loss appears in the temperature range from 1300 °C to 1400 °C, which has been attributed to the evaporation of Li_2O. The exothermic peaks observed at 1050 °C and at 1150 °C in the DTA curves, which are not accompanied by mass losses, probably correspond to the decomposition of the compounds. The melting point of the materials with x = 0.3 and x = 0.8 could not be clearly detected. Only the materials with x = 2.3 and x = 2.8 show three exothermic peaks, indicating a complex decomposition behavior between 950 °C and 1200 °C.

The sintering behavior of the calcined powders was examined by dilatometry. The pellets shrink up to ~23% between 1030 °C and 1220 °C. The sintering behavior is almost identical for all materials. With the exception of the samples with higher silicate content (x = 1.8, 2.3, and 2.8), which, as mentioned above, exhibit multiple-step shrinkage behavior, the other pellets show the onset of sintering between 850 °C (x = 0.3) and 950 °C (x = 0.8, 1.3) and the maximum shrinkage rate at about 1050 °C.

The pressed pellets were sintered at different temperatures to adjust the optimal sintering temperature for each composition. The sintering experiments in the furnace were carried out between $T_{10\%}$ and $T_{20\%}$, corresponding to 10% and 20% shrinkage in the dilatometry curves, in
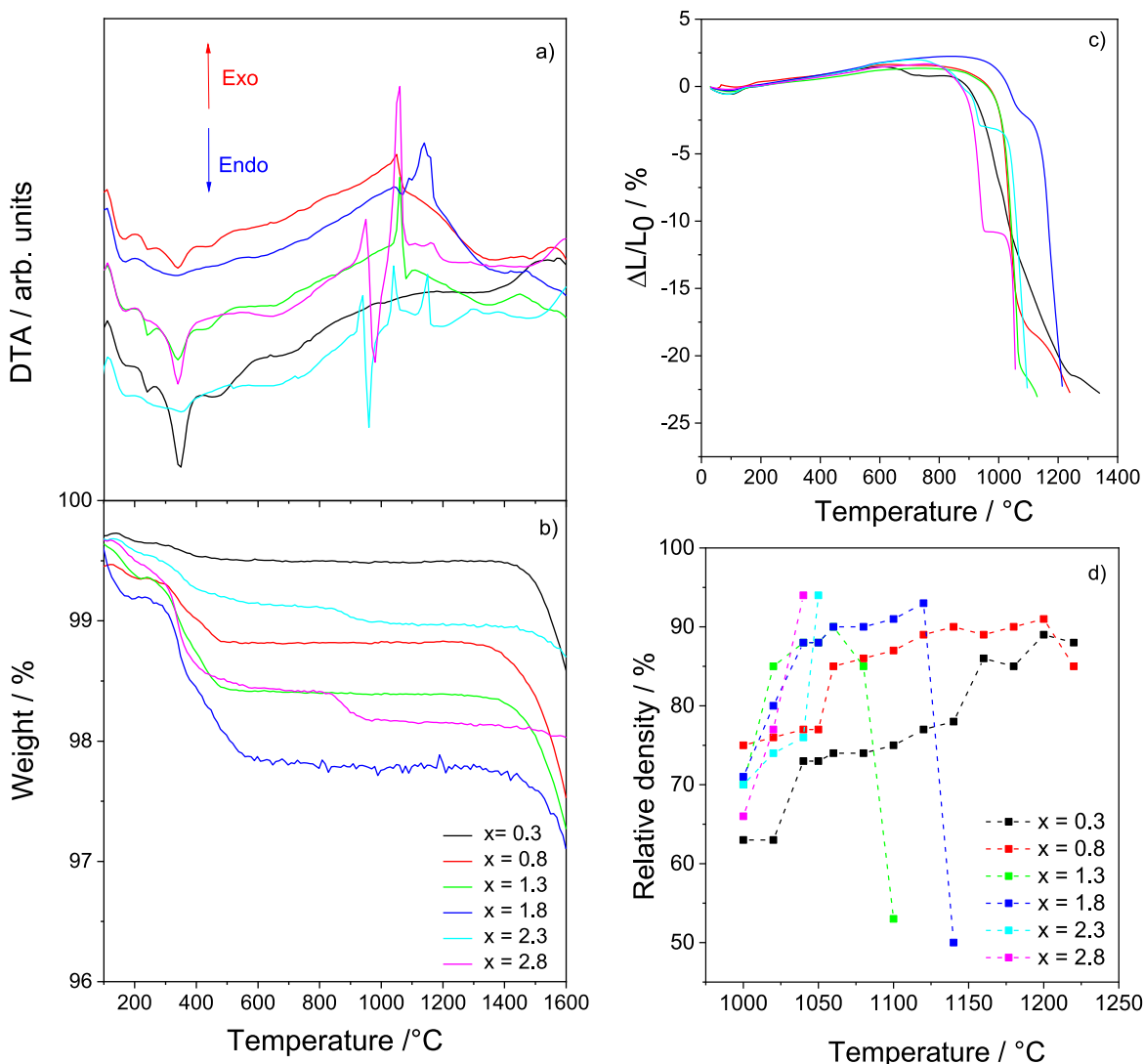
Fig. 8. Thermal and dilatometry investigations of the $Li_{1.2+x}Sc_{0.2}Zr_{1.8}Si_xP_{3-x}O_{12}$ series ($0.3 \leq x \leq 2.8$): a) DTA results, b) TG results, c) sintering curves with a constant heating rate up to 1400 °C, and d) relative densities obtained at different sintering temperatures after one-step sintering.

increments of 20 °C for 3 h in air. The resulting optimum sintering temperatures in relation to the densification of the materials are shown in Fig. 8d. The relative density increases gradually with increasing sintering temperature up to 1200 °C, and the highest densities of 89% and 91% were obtained for compositions with x = 0.3 and x = 0.8, respectively. The composition with x = 1.3 exhibited the highest relative density of 90% at 1060 °C and melted at 1070 °C.

Almost identical behavior was observed for the composition with x = 1.8, which exhibited the highest relative density of 93% at 1120 °C

and melted at 1140 °C. Materials with high silicate content (x = 2.3 and x = 2.8) showed the highest relative density of 94% at 1050 °C and 1040 °C, respectively, and melted at around 1060 °C. As an overall result, sintering of the pellets in the furnace at $T_{20\%}$ showed a high relative density for all compositions. Two-step sintering was also carried out with this set of compositions to improve the quality of the ceramics. The relative densities are summarized in Table 5. Increasing the partial anion substitution of silicate for phosphate in $Li_{1.2+x}Sc_{0.2}Zr_{1.8}Si_xP_{3-x}O_{12}$ lowered the sintering temperature from 1280 °C to 1200 °C (x = 0, see

Table 5

Melting points determined by DTA measurements, one-step sintering and two-step sintering parameters, and resulting densities of $Li_{1.2+x}Sc_{0.2}Zr_{1.8}Si_xP_{3-x}O_{12}$ ($0.3 \leq x \leq 2.8$) compounds. For comparison, the values for $Li_{1.2}Sc_{0.2}Zr_{1.8}P_3O_{12}$ are included (see Ref. [50]).

Composition	Melting temperature/°C	One-step sintering		Two-step sintering		
		T_s/°C, t_s/h	Relative density/%	T_{s1} (°C,t_{s1}/h)	T_{s2} (°C,t_{s2}/h)	T_s/°C, t_s/h
$Li_{1.2}Sc_{0.2}Zr_{1.8}P_3O_{12}$	1520	1280, 3	85	1280, 0.25	980, 3	94
$Li_{1.5}Sc_{0.2}Zr_{1.8}Si_{0.3}P_{2.7}O_{12}$	1380	1200, 3	89	1200, 0.25	800, 4	93
$Li_2Sc_{0.2}Zr_{1.8}Si_{0.8}P_{2.2}O_{12}$	1290	1200, 3	91	1200, 0.25	800, 4	94
$Li_{2.5}Sc_{0.2}Zr_{1.8}Si_{1.3}P_{1.7}O_{12}$	1070	1060, 3	90	1060, 0.25	800, 4	91
$Li_3Sc_{0.2}Zr_{1.8}Si_{1.8}P_{1.2}O_{12}$	1140	1120, 3	93	1120, 0.25	800, 4	94
$Li_{3.5}Sc_{0.2}Zr_{1.8}Si_{2.3}P_{0.7}O_{12}$	1060, 1160	1050, 3	94	1050, 0.25	800, 4	96
$Li_4Sc_{0.2}Zr_{1.8}Si_{2.8}P_{0.2}O_{12}$	1040, 1150	1040, 3	94	1040, 0.25	800, 4	95

Ref. [50], and x = 0.3, respectively) to 1040 °C with x = 2.8.

After sintering at temperatures associated with 20% shrinkage, the lithium content was slightly lower than the desired compositions (Fig. 9) due to weight losses during sintering. Nevertheless, this result is very promising with respect to the loss of Li_2O, since the evaporation of Li_2O was much higher for the $Li_{3+x}Sc_2Si_xP_{3-x}O_{12}$ series (Fig. 4). The substitution of phosphate with silicate in the $Li_{1.2+x}Sc_{0.2}Zr_{1.8}Si_xP_{3-x}O_{12}$ series lowered the sintering temperatures while reducing the evaporation of lithium species.

These results are in good agreement with the weight losses above 1200 °C in the DTA curves of both series, which were attributed to the evaporation of lithium oxide from the materials in the temperature range from 1300 °C to 1600 °C. The weight loss in the $Li_{3+x}Sc_2Si_xP_{3-x}O_{12}$ series was $\Delta m_3 \approx 2.58\%$, but only $\approx 1.53\%$ in the $Li_{1.2+x}Sc_{0.2}Zr_{1.8}Si_xP_{3-x}O_{12}$ series. Δm_3 was calculated according to equation (3) in the temperature interval mentioned above.

$$\Delta m_3 = \Sigma \frac{\Delta m_i}{n} \qquad \text{Equation 3}$$

with Δm_3 = mean value of the third mass loss of all compounds i, which is attributed to the evaporation of Li_2O from the materials, n = number of compounds.

The results show that Li_2O vaporization was affected by the sintering process and the presence of zirconium in the composition.

The XRD patterns of the materials $Li_{1.2+x}Sc_{0.2}Zr_{1.8}Si_xP_{3-x}O_{12}$ with 0.3 ≤ x ≤ 2.8 after sintering at temperatures listed in Table 5 are shown in Fig. 10. The patterns of the materials with 0.3 ≤ x ≤ 1.8 were refined with monoclinic.

NaSICON symmetry ($P2_1/n$) [29] and with orthorhombic symmetry (*Pbcn*) [53] (see also Tables S3 and S4 in the supporting information), since both phases are similar in their reflection patterns, as shown in Fig. 2. The results are in good agreement with the reported data for the composition $Li_3Sc_2(PO_4)_3$ [70]. The compositions with x = 2.3 only crystallized with monoclinic symmetry with ($P2_1/n$). The XRD patterns of the material with x = 2.8 exhibited complete decomposition.
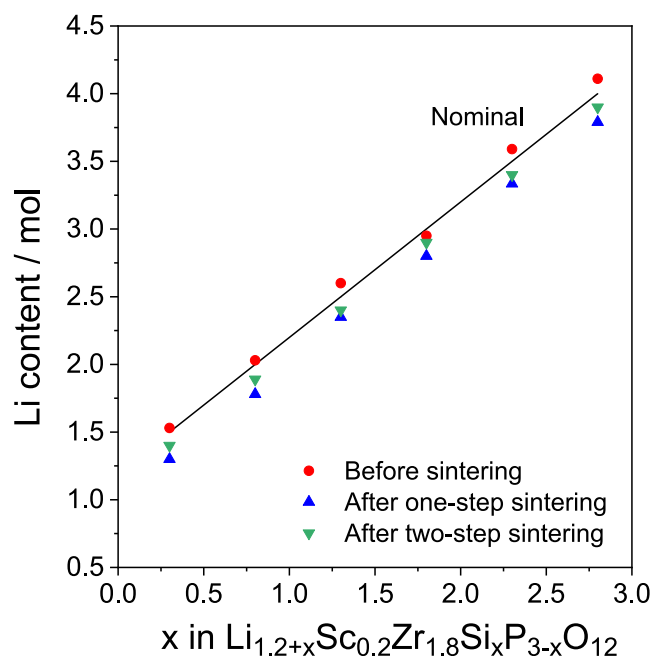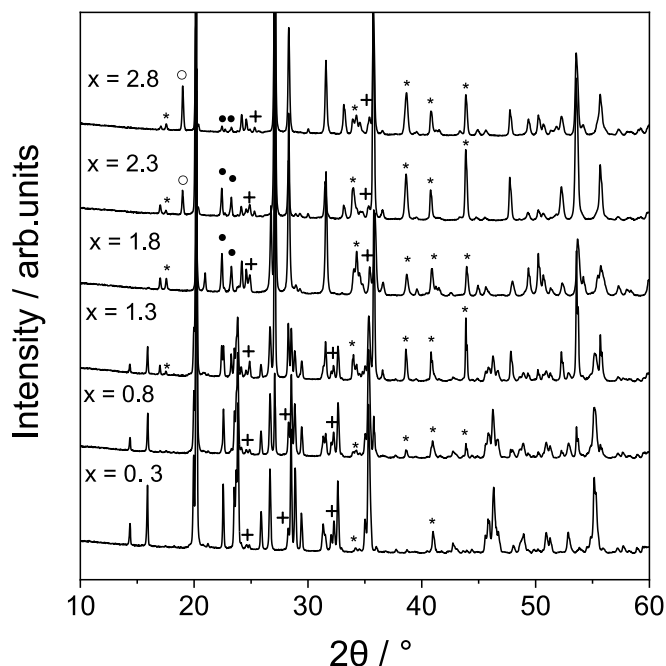

Fig. 10. XRD patterns of $Li_{1.2+x}Sc_{0.2}Zr_{1.8}Si_xP_{3-x}O_{12}$ with (0.3 ≤ x ≤ 2.8) after sintering at temperatures referring to the optimum densification: 1200 °C (x = 0.3, 0.8), 1060 °C (x = 1.3), 1120 °C (x = 1.8), 1050 °C (x = 2.3), 1040 °C (x = 2.8). +: ZrO_2, ●: Li_3PO_4, ○: Li_2SiO_3, *: $ZrSiO_4$.

The materials with x = 2.3 and x = 2.8 clearly show the presence of several secondary phases such as orthorhombic Li_3PO_4 with space group *Pmnb* (ICSD No. 50058), monoclinic ZrO_2 ($P2_1/c$; ICSD No. 60900) [72], and orthorhombic Li_2SiO_3 (*Ccm2₁*; ICSD No. 853) [73]. In addition, tetragonal $ZrSiO_4$ ($I4_1/amd$; ICSD No. 100243) [74] was also observed as an impurity phase in different amounts – not only for the decomposed materials (x = 2.3 and x = 2.8), but also for the compositions with 0.3 ≤ x ≤ 1.8. Using Rietveld refinements, the $ZrSiO_4$ content in materials with x = 0.3, 0.8, 1.3, 1.8, 2.3, and 2.8 was estimated to be 5, 11, 12, 14, 16, and 13 wt%, respectively (Table 6). From these values and the appearance of $ZrSiO_4$ over a wide range, it is clear that only a smaller fraction of the silicate substitution is incorporated in the NaSICON structure than expected. The molar amount of silicate in both phases can be calculated from the densities of $Li_{1.2}Sc_{0.2}Zr_{1.8}P_3O_{12}$ (3.09 g cm^{-3} [50]) and $ZrSiO_4$ (4.56 g cm^{-3} [73]) and the molar masses (Table 6). The silicate content in the NaSICON phase is always lower than the nominal value, and from the derived trend it can be deduced that coexistence with $ZrSiO_4$ starts at x < 0.2. These results indicate a continuous destabilization of the NaSICON materials along the series until decomposition occurs, which was detected at 960 °C and 980 °C in the DTA curves of the materials with x = 2.3 and x = 2.8, respectively, together with the various phases recorded by XRD.

Fig. 11 shows the variation of the refined cell parameters and cell volume of the $Li_{1.2+x}Sc_{0.2}Zr_{1.8}Si_xP_{3-x}O_{12}$ (0.3 ≤ x ≤ 1.8) series. The cell parameters were refined based on orthorhombic and monoclinic symmetry for the NaSICON phases. The converted monoclinic values of $Li_{1.2}Sc_{0.2}Zr_{1.8}P_3O_{12}$ (see Ref. [50]) are given for comparison.

In the orthorhombic system, a slight enlargement of the lattice is observed in the *a*, *b*, and *c* directions until x = 0.8, at which point the lattice shrinks again in all three directions. In the monoclinic system, the lattice parameters *a* and *c* are the first to show shrinkage, while the lattice parameter *b* remains almost constant. The cell volume decreases in both modifications, but decreases first in the monoclinic lattice from x = 0 to x = 0.2. The subsequent region of almost constant volume shows that the solubility limit for the silicate substitution is already reached at x = 0.2 and likely even earlier, since a small amount of $ZrSiO_4$ has

Fig. 9. Variation of lithium content obtained from ICP-OES in the $Li_{1.2+x}Sc_{0.2}Zr_{1.8}Si_xP_{3-x}O_{12}$ series with (0.3 ≤ x ≤ 2.8) before and after sintering. The results were normalized to 1.8 mol zirconium per formula unit. The pellets were sintered at temperatures listed in Table 5.

Table 6

Fractions of NaSICON polymorphs and impurities in the $Li_{1.2+x}Sc_{0.2}Zr_{1.8}Si_xP_{3-x}O_{12}$ series (in wt.%) as well as the molar distribution of silicate between $ZrSiO_4$ and the NaSICON phase.

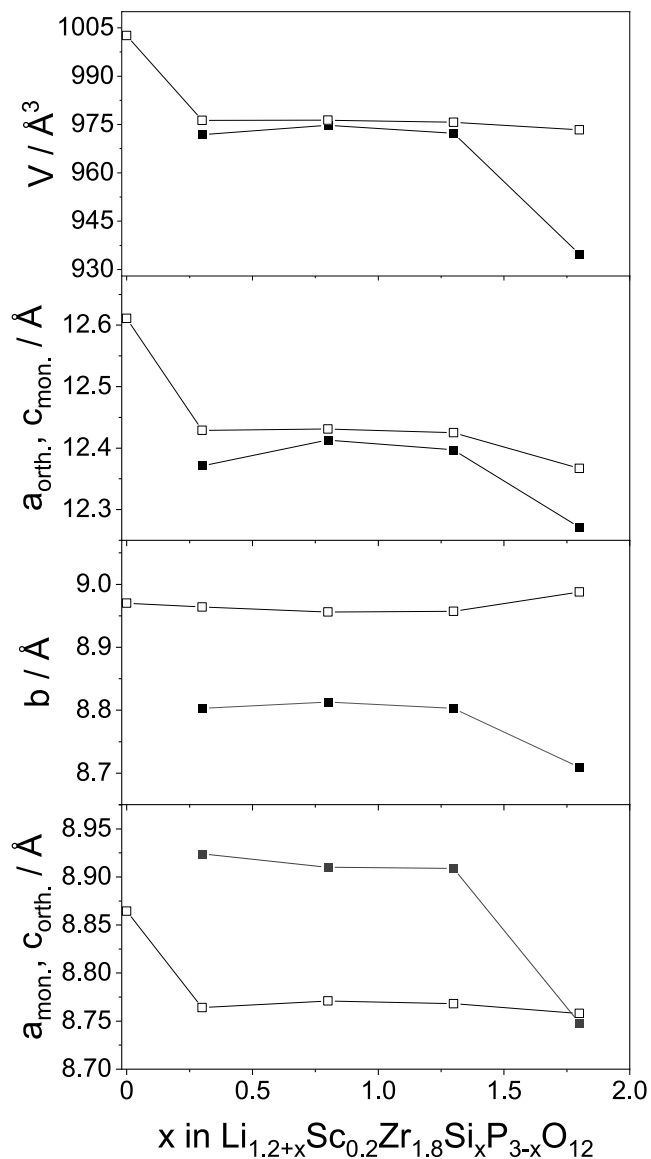| X	Mono-clinic/wt.%	Ortho-rhombic/wt.%	$ZrSiO_4$/wt.%	ZrO_2/wt.%	Li_3PO_4/wt.%	Li_2SiO_3/wt.%	$ZrSiO_4$/mol	Silicate in NaSICON/mol
0.3	40	55	5	0	0	0	0.12	0.18
0.8	42	47	11	0	0	0	0.24	0.56
1.3	48	40	12	0	0	0	0.26	1.04
1.8	55	31	14	0	0	0	0.29	1.51
2.3	68	0	16	8	6	2	–	–
2.8	Decomposition							

Fig. 11. Variation of orthorhombic (filled symbols) and monoclinic (open symbols) lattice parameters and unit cell volume in the $Li_{1.2+x}Sc_{0.2}Zr_{1.8}Si_xP_{3-x}O_{12}$ series ($0 \leq x \leq 1.8$).

Fig. 12. a) Nyquist plot of impedance spectra at 25 °C of $Li_{1.2+x}Sc_{0.2}Zr_{1.8}Si_xP_{3-x}O_{12}$ ($0.3 \leq x \leq 1.8$) after taking the sample dimensions into account. The equivalent circuit is also shown. b) Arrhenius plot of σ_t of $Li_{1.2+x}Sc_{0.2}Zr_{1.8}Si_xP_{3-x}O_{12}$ ($0.3 \leq x \leq 1.8$) measured in the temperature range of −40 °C–100 °C.

already been formed. The following volume decrease of the ortho-rhombic lattice between x = 0.3 and x = 1.8 can be interpreted as the first stage of destabilization of the NaSICON lattice. Impedance spectra were measured at 25 °C, and the Nyquist plots of $Li_{1.2+x}Sc_{0.2}Zr_{1.8}Si_xP_{3-x}O_{12}$ with $0.3 \leq x \leq 1.8$ are shown in Fig. 12. The fitted curves using the given equivalent circuit are also shown. For all samples, only one
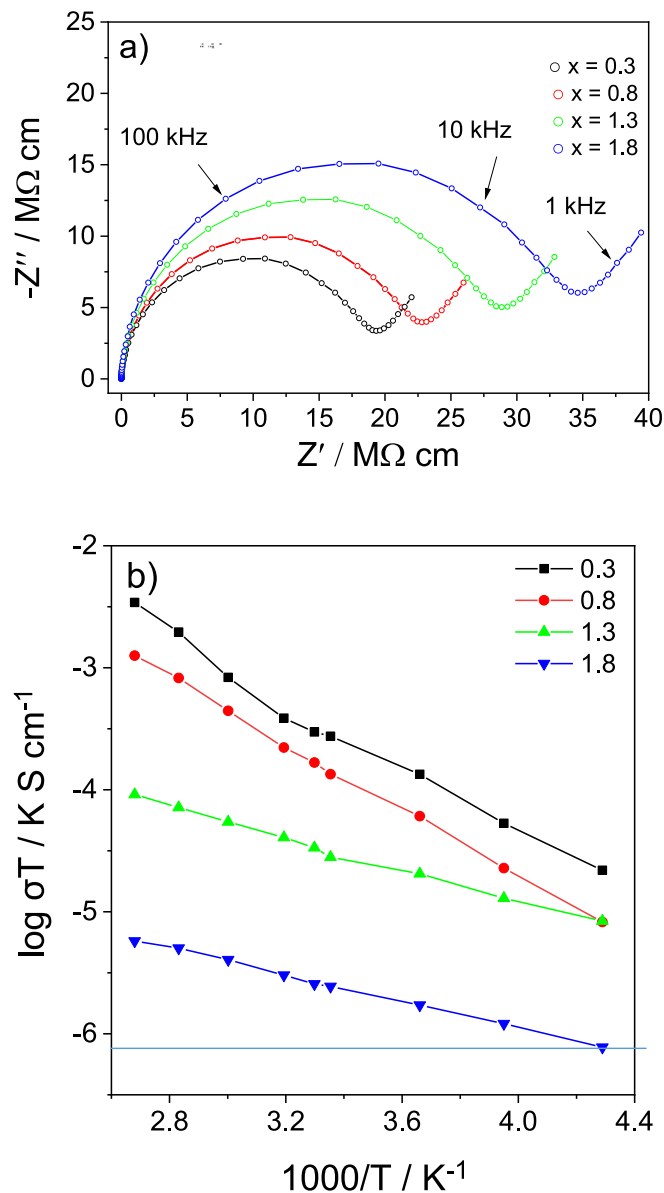
semicircle was observed at high frequencies, starting at the origin. The radius of the semicircle increases with increasing silicate substitution. The material $Li_{1.5}Sc_{0.2}Zr_{1.8}Si_{0.3}P_{2.7}O_{12}$ with the lowest silicate content (x = 0.3) thus shows the smallest R_t along the series. The total conductivity of the samples was calculated using Equation (1) and the

values are listed in Table 6.

The highest ionic conductivity (9.2×10^{-7} S cm^{-1}) is achieved for the material Li$_{1.5}$Sc$_{0.2}$Zr$_{1.8}$Si$_{0.3}$P$_{2.7}$O$_{12}$ with the lowest silicate content, and any further increase in silicate content leads to a sharp decrease in ionic conductivity. In contrast, the silicate-free material Li$_{1.2}$Sc$_{0.2}$Zr$_{1.8}$P$_3$O$_{12}$ has a higher conductivity than Li$_{1.5}$Sc$_{0.2}$Zr$_{1.8}$Si$_{0.3}$P$_{2.7}$O$_{12}$ (Table 6), showing that substitution with (SiO$_4$)$^{4-}$ is not beneficial throughout the series. These results are consistent with the XRD studies. The excess of non-substituting silicate forms a large amount of ZrSiO$_4$, as is clear from the XRD patterns in Fig. 10, starting with the material Li$_{1.5}$Sc$_{0.2}$Zr$_{1.8}$Si$_{0.3}$P$_{2.7}$O$_{12}$, which only has two peaks assigned to ZrSiO$_4$. The increasing amounts of precipitates of Li$_3$PO$_4$, ZrO$_2$, Li$_2$SiO$_3$, and ZrSiO$_4$ have a significantly negative influence on ionic conductivity.

Among the materials of the Li$_{3+x}$Sc$_2$Si$_x$P$_{3-x}$O$_{12}$ series ($0 \leq x \leq 0.6$), Li$_{3.15}$Sc$_2$Si$_{0.15}$P$_{2.85}$O$_{12}$ shows the highest ionic conductivity (1.2×10^{-5} S cm^{-1}) at 25 °C with a relative density of 93% after sintering in two steps at 1000 °C and 800 °C for 0.25 h and 4 h, respectively. The analogous series with sodium-based NaSICON materials, i.e. Na$_{3+x}$Sc$_2$Si$_x$P$_{3-x}$O$_{12}$ with $0 < x < 0.8$ [75,76], was investigated earlier and showed increasing conductivity before reaching a maximum at x = 0.4, after which point there was an unfavorable ratio of the amount of charge carriers to vacancies. The Na$_{3.4}$Sc$_2$Si$_{0.4}$P$_{2.6}$O$_{12}$ material crystallized with the rhombohedral structure, and an ionic conductivity of 6.9×10^{-4} S cm^{-1} at 25 °C was reported with a relative density of 92 %.

The material with x = 0 in the Li$_{1.2+x}$Sc$_{0.2}$Zr$_{1.8}$Si$_x$P$_{3-x}$O$_{12}$ series ($0 \leq x \leq 2.8$) showed the highest ionic conductivity (4.8×10^{-5}) at 25 °C with a relative density of 94%. An almost identical series of sodium-based NaSICON materials with the formula Na$_{3+x}$Sc$_x$Zr$_{2-x}$Si$_2$PO$_{12}$ ($0 \leq x \leq 0.6$) was reported by Ma et al. [51]. An optimum total ionic conductivity of 4.0×10^{-3} S cm^{-1} at 25 °C was achieved with Na$_{3.4}$Sc$_{0.4}$Zr$_{1.6}$Si$_2$PO$_{12}$; a relative density of 95% was obtained by free sintering at 1260 °C for 5 h. The XRD patterns of this compound show the presence of a mixture with 55 and 45% of monoclinic and rhombohedral symmetry, respectively.

The comparison of lithium-based NaSICON materials with sodium-based analogues shows that the highest values of ionic conductivity can be obtained with the sodium-based NaSICON materials [51,75,76], and we can conclude that the materials with zirconium in their structure have a higher ionic conductivity than materials with scandium.

The activation energy E$_a$ of the ionic conductivity of all compounds except x = 2.3 and 2.8 was obtained from impedance measurements in the temperature range of −40 °C–100 °C as shown in Fig. 12b and summarized in Table 7. The E$_a$ of Li$_{1.2+x}$Sc$_{0.2}$Zr$_{1.8}$Si$_x$P$_{3-x}$O$_{12}$ ($0.3 \leq x \leq 1.8$) specimens decrease from 0.26 eV to 0.11 eV with increasing x. Whereas the E$_a$ values for x = 0.3 and 0.8 are again in good agreement with previous work, the samples with x = 13 and 1. 8 show exceptionally low activation energies. These low activation energies may be explained with the increasing amount of ZrSiO$_4$ which leads to an excess of lithium oxide in the matrix, the formation of additional lithium compounds and, hence, to an enhanced hygroscopicity of the samples. Therefore it cannot be excluded that the low E$_a$ values in combination with the low ionic conductivities are a result of mixed Li$^+$/H$^+$ conductivity.

4. Conclusions

Materials of the Li$_{3+x}$Sc$_2$Si$_x$P$_{3-x}$O$_{12}$ series with $0 \leq x \leq 0.6$ derived from the parent compound Li$_3$Sc$_2$(PO$_4$)$_3$ and the partial substitution of P^{5+} with Si^{4+} in the Li$_{1.2+x}$Sc$_{0.2}$Zr$_{1.8}$Si$_x$P$_{3-x}$O$_{12}$ system with $0 \leq x \leq 2.8$ were prepared via solution-assisted solid-state reaction. Rietveld refinement of room temperature powder XRD patterns revealed the incidence of mixed orthorhombic and monoclinic symmetry in all cases. Optimizing the sintering conditions through two-step sintering led to enhanced relative density and limited Li$_2$O loss because the sample is exposed to shorter durations at high temperature (depending on composition) and increased ionic conductivity. The total ionic

Table 7

Ionic conductivity at 25 °C and activation energy for Li$_{1.2+x}$Sc$_{0.2}$Zr$_{1.8}$Si$_x$P$_{3-x}$O$_{12}$ ($0.3 \leq x \leq 1.8$). For comparison, the $\sigma_{25°C}$ value of Li$_{1.2}$Sc$_{0.2}$Zr$_{1.8}$P$_3$O$_{12}$ is included (see Ref. [50]).

X	Relative density/%	$\sigma_{25°C}$/S cm^{-1}	Activation energy/eV
0	94	4.8×10^{-5}	–
0.3	93	9.2×10^{-7}	0.26
0.8	94	4.5×10^{-7}	0.27
1.3	91	9.4×10^{-8}	0.13
1.8	94	8.2×10^{-9}	0.11

conductivity initially increases with increasing x in the Li$_{3+x}$Sc$_2$Si$_x$P$_{3-x}$O$_{12}$ series and the maximum value of conductivity (1.2×10^{-5} S cm^{-1}) was obtained with Li$_{3.15}$Sc$_2$Si$_{0.15}$P$_{2.85}$O$_{12}$. This trend can be mainly attributed to the substitution of silicate in Li$_{3+x}$Sc$_2$Si$_x$P$_{3-x}$O$_{12}$ and the additional Li$^+$ ions needed for charge balance. Consequently, more lithium ions led to a significant improvement in ionic conductivity. Although the ionic conductivity was improved along the series, it still remains a level that is unfavorable for battery application.

The series Li$_{1.2+x}$Sc$_{0.2}$Zr$_{1.8}$Si$_x$P$_{3-x}$O$_{12}$ was synthesized for the first time and the highest ionic conductivity was achieved for the material Li$_{1.5}$Sc$_{0.2}$Zr$_{1.8}$Si$_{0.3}$P$_{2.7}$O$_{12}$ with the lowest silicate content (9.2×10^{-7} S cm^{-1}). Any further increase in silicate content leads to a sharp decrease in ionic conductivity. Therefore, it can be concluded that this Zr-containing series showed the highest ionic conductivity without silicate substitution. Because of the increasing amounts of additional phases, the substitution with (SiO$_4$)$^{4-}$ is not beneficial throughout the series.

For comparison, the total ionic conductivity of Na$_{3.4}$Sc$_{0.4}$Zr$_{1.6}$Si$_2$PO$_{12}$ is 4.0×10^{-3} S cm^{-1} at 25 °C in the analogous series of sodium-based NaSICON materials, which is one of the best values of all sodium-based NaSICON materials. In addition and in contrast to the Li-NaSICONs, a complete substitution with (SiO$_4$)$^{4-}$ can be achieved without Sc substitution. This shows that the larger Na$^+$ ion can better stabilize the Zr-containing NaSICON structure and can also better tolerate polyanionic substitutions.

Declaration of interest statement

The authors declare no conflict of interest, and they have no established conflicting financial interests or personal relationships that may have influenced the research presented in this paper.

Acknowledgements

Appendix A. Supplementary data

Supplementary data to this article can be found online at https://doi.org/10.1016/j.oceram.2022.100313.

References

[1] F. Wu, J. Maier, Y. Ya, Guidelines and trends for next-generation rechargeable lithium and lithium-ion batteries, Chem. Soc. Rev. 49 (2020) 1569–1614.

[2] C. Sun, J. Liu, Y. Gong, D.P. Wilkinson, J. Zhang, Recent advances in all-solid-state rechargeable lithium batteries, Nano Energy 33 (2017) 363–386.

[3] S. Randau, D.A. Weber, O. Kötz, R. Koerver, P. Braun, A. Weber, E. Ivers-Tiffée, T. Adermann, J. Kulisch, W.G. Zeier, Benchmarking the performance of all-solid-state lithium batteries, Nat. Energy 5 (2020) 259–270.

[4] R. Chen, Q. Li, X. Yu, L. Chen, H. Li, Approaching practically accessible solid-state batteries: stability issues related to solid electrolytes and interfaces, Chem. Rev. 120 (2019) 6820–6877.

[5] D.T. Hallinan, I. Villaluenga, N.P. Balsara, Polymer and composite electrolytes, MRS Bull. 43 (2018) 759–767.

[6] L. Long, Polymer electrolytes for lithium polymer batteries, J. Mater. Chem. A 4 (2016) 10038–10069.

[7] Z. Zhang, Y. Shao, B. Lotsch, Y.S. Hu, H. Li, J. Janek, L.F. Nazar, C.W. Nan, J. Maier, M. Armand, New horizons for inorganic solid state ion conductors, Energy Environ. Sci. 11 (2018) 1945–1976.

[8] P.J. Lian, B.S. Hao, L.Q. Zhang, N. Xu, M.T. Wu, X.P. Gao, Inorganic sulfide solid electrolytes for all-solid-state lithium secondary batteries, J. Mater. Chem. A 7 (2019) 20540–20557.

[9] J.C. Bachman, S. Muy, A. Grimaud, H.H. Chang, N. Pour, S.F. Lux, O. Paschos, F. Maglia, S. Lupart, P. Lamp, Inorganic solid-state electrolytes for lithium batteries: mechanisms and properties governing ion conduction, Chem. Rev. 116 (2016) 140–162.

[10] M. Hou, F. Liang, K. Chen, Y. Dai, D. Xue, Challenges and perspectives of NaSICON-type solid electrolytes for all-solid-state lithium batteries, Nanotechnology 31 (2020), 132003.

[11] J. Dai, C. Yang, C. Wang, G. Pastel, L. Hu, Interface engineering for Garnet-based solid-state lithium-metal batteries: materials, structures, and characterization, Adv. Mater. 30 (2018), 1802068.

[12] H. Aono, N. Imanaka, G. Adachi, High Li$^+$ conducting ceramics, Accounts Chem. Res. 27 (1994) 265–270.

[13] H. Aono, E. Sugimoto, Y. Sadaoka, N. Imanaka, G.Y. Adachi, Ionic conductivity of solid electrolytes based on lithium titanium phosphate, J. Electrochem. Soc. 137 (1990) 1023–1027.

[14] J.A. Dias, S.H. Santagneli, Y. Messaddeq, Methods for lithium ion NaSICON preparation: from solid-state synthesis to highly conductive glass-ceramics, J. Phys. Chem. C 124 (2020) 26518–26539.

[15] Y.H. Rho, K. Kanamura, Fabrication of all solid-state rechargeable lithium battery and its electrochemical properties, J. Power Sources 158 (2006) 1436–1441.

[16] K. Dokko, K. Hoshina, H. Nakano, K. Kanamura, Preparation of LiMn$_2$O$_4$ thin-film electrode on Li$_{1+x}$Al$_x$Ti$_{2-x}$(PO$_4$)$_3$ NaSICON-type solid electrolyte, J. Power Sources 174 (2007) 1100–1103.

[17] E. Kobayashi, L.S. Plashnitsa, T. Doi, S. Okada, J.I. Yamaki, Electrochemical properties of Li symmetric solid-state cell with NaSICON-type solid electrolyte and electrodes, Electrochem. Commun. 12 (2010) 894–896.

[18] H. Morimoto, M. Hirukawa, A. Matsumoto, T. Kurahayashi, N. Ito, S.I. Tobishima, Lithium ion conductivities of NaSICON-type Li$_{1+x}$Al$_x$Ti$_{2-x}$(PO$_4$)$_3$ solid electrolytes prepared from amorphous powder using a mechanochemical method, Electrochemistry 82 (2014) 870–874.

[19] M. Cretin, P. Fabry, Comparative study of lithium ion conductors in the system Li$_{1+x}$Al$_x$A$_{2-x}$IV(PO$_4$)$_3$ with AIV= Ti or Ge and $0 \le x \le 0.7$ for use as Li$^+$ sensitive membranes, J. Eur. Ceram. Soc. 19 (1999) 2931–2940.

[20] A. Rossbach, F. Tietz, S. Grieshammer, Structural and transport properties of lithium-conducting NaSICON materials, J. Power Sources 391 (2018) 1–9.

[21] F. Zheng, M. Kotobuki, S. Song, M.O. Lai, L. Lu, Review on solid electrolytes for all-solid-state lithium-ion batteries, J. Power Sources 389 (2018) 198–213.

[22] B. Davaasuren, F. Tietz, Impact of sintering temperature on phase formation, microstructure, crystallinity and ionic conductivity of Li$_{1.5}$Al$_{0.5}$Ti$_{1.5}$(PO$_4$)$_3$, Solid State Ionics 338 (2019) 144–152.

[23] Q. Ma, Q. Xu, C.L. Tsai, F. Tietz, O. Guillon, A novel sol–gel method for large-scale production of nanopowders: preparation of Li$_{1.5}$Al$_{0.5}$Ti$_{1.5}$(PO$_4$)$_3$ as an example, J. Am. Ceram. Soc. 99 (2016) 410–414.

[24] P. Zhang, M. Matsui, A. Hirano, Y. Takeda, O. Yamamoto, N. Imanishi, Water-stable lithium ion conducting solid electrolyte of the Li$_{1.4}$Al$_{0.4}$Ti$_{1.6-x}$Ge$_x$(PO$_4$)$_3$ system (x = 0 - 1.0) with NaSICON-type structure, Solid State Ionics 253 (2013) 175–180.

[25] S.C. Li, J.Y. Cai, Z.X. Lin, Phase relationships and electrical conductivity of Li$_{1+x}$Ge$_{2-x}$Al$_x$(PO$_4$)$_3$ and Li$_{1+x}$Ge$_{2-x}$Cr$_x$(PO$_4$)$_3$ systems, Solid State Ionics (1988) 1265–1270.

[26] P. Maldonado-Manso, M.C. Martín-Sedeño, S. Bruque, J. Sanz, E.R. Losilla, Unexpected cationic distribution in tetrahedral/octahedral sites in nominal Li$_{1+x}$Ge$_{2-x}$Al$_x$(PO$_4$)$_3$ NaSICON series, Solid State Ionics 178 (2007) 43–52.

[27] L. Castro, E. Petit, A. Benayad, F. Mauvy, B. Pecquenard, F. Le Cras, C. Barchasz, Evaluation of chemical stability of conducting ceramics to protect metallic lithium in Li/S batteries, Solid State Ionics 354 (2020), 115402.

[28] W.D. Richards, L.J. Miara, Y. Wang, J.C. Kim, G. Ceder, Interface stability in solid-state batteries, Chem. Mater. 28 (2016) 266–273.

[29] Y. Liu, Q. Sun, Y. Zhao, B. Wang, P. Kaghazchi, K.P. Adair, R. Li, C. Zhang, J. Liu, L. Y. Kuo, Stabilizing the interface of NaSICON solid electrolyte against Li metal with atomic layer deposition, ACS Appl. Mater. Interfaces 10 (2018) 31240–31248.

[30] M. Sato, T. Suzuki, K. Yoshida, K. Uematsu, K. Toda, Z.G. Ye, Synthesis and properties of lithium ion conductors Li$_{3-2x}$(Sc$_{1-x}$Zr$_x$)$_2$(PO$_4$)$_3$, J. Alloys Compd. 250 (1997) 510–514.

[31] T. Suzuki, K. Yoshida, K. Uematsu, T. Kodama, K. Toda, Z.G. Ye, M. Ohashi, M. Sato, Structure refinement of lithium ion conductors Li$_3$Sc$_2$(PO$_4$)$_3$ and Li$_{3-2x}$(Sc$_{1-x}$M$_x$)$_2$(PO$_4$)$_3$ (M = Ti, Zr) with x = 0.10 by neutron diffraction, Solid State Ionics 113 (1998) 89–96.

[32] Y. Li, M. Liu, K. Liu, C.A. Wang, High Li$^+$ conduction in NaSICON-type Li$_{1+x}$Y$_x$Zr$_{2-x}$(PO$_4$)$_3$ at room temperature, J. Power Sources 240 (2013) 50–53.

[33] T. Šalkus, A. Kežionis, V. Kazlauskienė, J. Miškinis, A. Dindune, Z. Kanepe, J. Ronis, A.F. Orliukas, Surface and impedance spectroscopy studies of Li$_{2.8}$Sc$_{1.8-}$

[34] yY$_y$Zr$_{0.2}$(PO$_4$)$_3$ (where y = 0, 0.1) solid electrolyte ceramics, Mater. Sci. Eng., B 172 (2010) 156–162.

[34] T. Savitha, S. Selvasekarapandian, C. Ramya, Structural and electrical conductivity studies of Li$_x$AlZr[PO$_4$]$_3$ (x= 1.8, 2.0, 2.2), solid electrolyte for lithium-rechargeable batteries, J. Solid State Electrochem. 12 (2008) 857–860.

[35] Y. Zhang, K. Chen, Y. Shen, Y. Lin, C.W. Nan, Enhanced lithium-ion conductivity in a LiZr$_2$(PO$_4$)$_3$ solid electrolyte by Al doping, Ceram. Int. 43 (2017) S598–S602.

[36] H. Xie, J.B. Goodenough, Y. Li, Li$_{1.2}$Zr$_{1.9}$Ca$_{0.1}$(PO$_4$)$_3$, a room-temperature Li-ion solid electrolyte, J. Power Sources 196 (2011) 7760–7762.

[37] A. Cassel, B. Fleutot, M. Courty, V. Viallet, M. Morcrette, Sol-gel synthesis and electrochemical properties extracted by phase inflection detection method of NaSICON-type solid electrolytes LiZr$_2$(PO$_4$)$_3$ and Li$_{1.2}$Zr$_{1.9}$Ca$_{0.1}$(PO$_4$)$_3$, Solid State Ionics 309 (2017) 63–70.

[38] S. Kumar, P. Balaya, Improved ionic conductivity in NaSICON-type Sr^{2+} doped LiZr$_2$(PO$_4$)$_3$, Solid State Ionics 296 (2016) 1–6.

[39] S. Smith, T. Thompson, J. Sakamoto, J.L. Allen, D.R. Baker, J. Wolfenstine, Electrical, mechanical and chemical behavior of Li$_{1.2}$Zr$_{1.9}$Sr$_{0.1}$(PO$_4$)$_3$, Solid State Ionics 300 (2017) 38–45.

[40] M. Sugantha, U.V. Varadaraju, Ionic conductivity of Li$^+$ ion conductors Li$_2$M^{3+}M^{4+}(PO$_4$)$_3$, Solid State Ionics 95 (1997) 201–205.

[41] B. Maksimov, L.A. Muradyan, E.A. Genkina, V.I. Simonov, Crystal structure of the monoclinic modification of Li$_3$Fe$_2$(PO$_4$)$_3$, in: Soviet Physics Doklady, 1986.

[42] K. Arbi, M. Ayadi-Trabelsi, J. Sanz, Li mobility in triclinic and rhombohedral phases of the Nasicon-type compound LiZr$_2$(PO$_4$)$_3$ as deduced from NMR spectroscopy, J. Mater. Chem. 12 (2002) 2985–2990.

[43] C. Mariappan, P. Kumar, A. Kumar, S. Indris, H. Ehrenberg, G.V. Prakash, R. Jose, Ionic conduction and dielectric properties of yttrium doped LiZr$_2$(PO$_4$)$_3$ obtained by a Pechini-type polymerizable complex route, Ceram. Int. 44 (2018) 15509–15516.

[44] T. Hupfer, E.C. Bucharsky, K.G. Schell, A. Senyshyn, M. Monchak, M.J. Hoffmann, H. Ehrenberg, Evolution of microstructure and its relation to ionic conductivity in Li$_{1+x}$Al$_x$Ti$_{2-x}$(PO$_4$)$_3$, Solid State Ionics 288 (2016) 235–239.

[45] E.D. Case, The effect of microcracking upon the Poisson's ratio for brittle materials, J. Mater. Sci. 19 (1984) 3702–3712.

[46] E. Antolini, Lithium loss kinetics from polycrystalline Li$_x$Ni$_{1-x}$O at high temperatures, J. Mater. Chem. 8 (1998) 2783–2786.

[47] H. Bai, J. Hu, X. Li, Y. Duan, F. Shao, T. Kozawa, M. Naito, J. Zhang, Jingxian, Influence of LiBO$_2$ addition on the microstructure and lithium-ion conductivity of Li$_{1+x}$Al$_x$Ti$_{2-x}$(PO$_4$)$_3$ (x = 0.3) ceramic electrolyte, Ceram. Int. 44 (2018) 6558–6563.

[48] P. Hui-Fen, G. Mei-Ling, W. Ming-Fang, Effect of annions substitutions of SiO$_4$ for Li$_3$Sc$_2$(PO$_4$)$_3$ superion conductor, Chin. J. Inorg. Chem. 27 (2011) 1969–1974.

[49] W. Belam, A. Essoumhi, P. Satre, Synthesis and physico-chemical characterizations of the lithium-substituted NaSICONS series with general formula Li$_{2.8}$Zr$_{2-y}$Si$_{1.8-4y}$P$_{1.2+4y}$O$_{12}$ where ($0 \le y \le 0.45$), Z. Phys. Chem. 221 (2007) 225–234.

[50] A. Loutati, P. Odenwald, B. Aktekin, J. Sann, O. Guillon, F. Tietz, D. Fattakhova-Rohlfing, Survey of zirconium-containing NaSICON-type solid-state Li$^+$ ion conductors with the aim of increasing reduction stability by partial cation substitution, Batter. Supercaps (2022), e202200327.

[51] Q. Ma, M. Guin, S. Naqash, C.L. Tsai, F. Tietz, O. Guillon, Scandium-substituted Na$_3$Zr$_2$(SiO$_4$)$_2$(PO$_4$) prepared by a solution-assisted solid-state reaction method as sodium-ion conductors, Chem. Mater. 28 (2016) 4821–4828.

[52] H.P. Hong, Crystal structures and crystal chemistry in the system Na$_{1+x}$Zr$_2$SixP$_{3-x}$O$_{12}$, Mater. Res. Bull. 11 (1976) 173–182.

[53] M. Catti, N. Morgante, R.M. Ibberson, Order–disorder and mobility of Li$^+$ in the β′-and β-LiZr$_2$(PO$_4$)$_3$ ionic conductors: a neutron diffraction study, J. Solid State Chem. 152 (2000) 340–347.

[54] B. Maksimov, L.A. Muradyan, N.N. Vydanov, V.A. Sarin, A.B. Bykov, Neutron-diffraction refinement of atomic structure of α-and γ-phases of crystals of Li$_3$Sc$_2$(PO$_4$)$_3$ at 293 and 573 K, Soviet Physics, Crystallography 36 (1991) 810–816.

[55] B. Maksimov, L.A. Muradyan, E.A. Genkina, I.A. Verin, Crystal structure of Li$_3$Sc$_2$(PO$_4$)$_3$ at 573 K, Kristallografiya 31 (1986) 592–594.

[56] A. Bykov, A.P. Chirkin, L.N. Demyanets, S.N. Doronin, E.A. Genkina, A.K. Ivanov-Shits, I.P. Kondratyuk, B.A. Maksimov, O.K. Mel'Nikov, L.N. Muradyan, Superionic conductors Li$_3$M$_2$(PO$_4$)$_3$ (M = Fe, Sc, Cr): synthesis, structure and electrophysical properties, Solid State Ionics 38 (1990) 31–52.

[57] E. McCalla, G.H. Carey, J.R. Dahn, Lithium loss mechanisms during synthesis of layered Li$_x$Ni$_{2-x}$O$_2$ for lithium ion batteries, Solid State Ionics 219 (2012) 11–19.

[58] A. Loutati, Y.J. Sohn, F. Tietz, Phase-field determination of NaSICON materials in the quaternary system Na$_2$O–P$_2$O$_5$–SiO$_2$–ZrO$_2$: the series Na$_3$Zr$_{3-x}$Si$_2$P$_x$O$_{11.5+x/2}$, ChemPhysChem 22 (2021) 995–1007.

[59] P. Feng, M. Niu, C. Gao, S. Peng, C. Shuai, A novel two-step sintering for nano-hydroxyapatite scaffolds for bone tissue engineering, Sci. Rep. 4 (2014) 1–10.

[60] M. Mazaheri, A. Simchi, F. Golestani-Fard, Densification and grain growth of nanocrystalline 3Y-TZP during two-step sintering, J. Eur. Ceram. Soc. 28 (2008) 2933–2939.

[61] M. Ihrig, M. Finsterbusch, C.L. Tsai, A.M. Laptev, C.H. Tu, M. Bram, Y.J. Sohn, R. Ye, S. Sevinc, S.K. Lin, Low temperature sintering of fully inorganic all-solid-state batteries impact of interfaces on full cell performance, J. Power Sources 482 (2021), 228905.

[62] C.W. Ban, G.M. Choi, The effect of sintering on the grain boundary conductivity of lithium lanthanum titanates, Solid State Ionics 140 (2001) 285–292.

[63] H. Rieck, R. Hoppe, Ein neues oxoniccolat: Li$_2$NiO$_2$, Z. Anorg. Allg. Chem. 392 (1972) 193–196.

[64] S. Hasegawa, N. Imanishi, T. Zhang, J. Xie, A. Hirano, Y. Takeda, O. Yamamoto, Study on lithium/air secondary batteries-Stability of NaSICON-type lithium ion conducting glass-ceramics with water, J. Power Sources 189 (2009) 371–377.

[65] M. Bagieu-Beucher, J.C. Guitel, Affinement de la structure cristalline du tétramétaphosphate de scandium: $Sc_4(P_4O_{12})_3$, Acta Crystallogr. Sect. B Struct. Crystallogr. Cryst. Chem. 34 (1978) 1439–1442.

[66] D.W.J. Cruickshank, Refinements of structures containing bonds between Si, P, S or Cl and O or N. V. P_4O_{10}, Acta Crystallogr. 17 (1964) 677–679.

[67] B. Wu, M. Zinkevich, F. Aldinger, D. Wen, L. Chen, Ab initio study on structure and phase transition of A-and B-type rare-earth sesquioxides Ln_2O_3 (Ln = La–Lu, Y, and Sc) based on density function theory, J. Solid State Chem. 180 (2007) 3280–3287.

[68] R.D. Shannon, Revised effective ionic radii and systematic studies of interatomic distances in halides and chalcogenides, Acta Crystallogr. Sect. A Cryst. Phys. Diffr. Theor. Gen. Crystallogr. 32 (1976) 751–767.

[69] G. Amatucci, A. Safari, F.K. Shokoohi, B.J. Wilkens, Lithium scandium phosphate-based electrolytes for solid state lithium rechargeable microbatteries, Solid State Ionics 60 (1993) 357–365.

[70] T. Suzuki, K. Yoshida, K. Uematsu, T. Kodama, K. Toda, Z.G. Ye, M. Sato, Stabilization of superionic conduction phase in $Li_3Sc_2(PO_4)_3$, Solid State Ionics 104 (1997) 27–33.

[71] S.E. Sigaryov, E.A. Genkina, B.A. Maximov, Some features of Li^+ ion distribution in monoclinic modifications of $Li_3M_2(PO_4)_3$ (M= Sc, Fe, In) superionic conductors, Solid State Ionics 37 (1990) 261–265.

[72] R.E. Hann, P.R. Suitch, J.L. Pentecost, Monoclinic crystal structures of ZrO_2 and HfO_2 refined from X-ray powder diffraction data, J. Am. Ceram. Soc. 68 (1985). C-285-C-286.

[73] K.F. Hesse, Refinement of the crystal structure of lithium polysilicate, Acta Crystallogr. Sect. B Struct. Crystallogr. Cryst. Chem. 33 (1977) 901–902.

[74] R.M. Hazen, L.W. Finger, Crystal structure and compressibility of zircon at high pressure, Am. Mineral. 64 (1979) 196–201.

[75] M. Guin, E. Dashjav, C.M.N. Kumar, F. Tietz, O. Guillon, Investigation of crystal structure and ionic transport in a scandium-based NaSICON material by neutron powder diffraction, Solid State Sci. 67 (2017) 30–36.

[76] M. Guin, F. Tietz, O. Guillon, New promising NaSICON material as solid electrolyte for sodium-ion batteries: correlation between composition, crystal structure and ionic conductivity of $Na_{3+x}Sc_2Si_xP_{3-x}O_{12}$, Solid State Ionics 293 (2016) 18–26.